Redox-mediated electrochemical separation of boron ions

Cell design, process optimization, adsorption isotherm, kinetics, and thermodynamics

Polat, Sevgi; Eral, Hüseyin Burak

DOI
10.1016/j.jwpe.2024.106481

Publication date
2024

Document Version
Final published version

Published in
Journal of Water Process Engineering

Citation (APA)
Polat, S., & Eral, H. B. (2024). Redox-mediated electrochemical separation of boron ions: Cell design, process optimization, adsorption isotherm, kinetics, and thermodynamics. *Journal of Water Process Engineering*, *68*, Article 106481. https://doi.org/10.1016/j.jwpe.2024.106481

Journal of Water Process Engineering 68 (2024) 106481

Contents lists available at ScienceDirect

Journal of Water Process Engineering

journal homepage: www.elsevier.com/locate/jwpe

Redox-mediated electrochemical separation of boron ions: Cell design, process optimization, adsorption isotherm, kinetics, and thermodynamics

Sevgi Polat [a,b,*], Hüseyin Burak Eral [b]

[a] Chemical Engineering Department, Faculty of Engineering, Marmara University, 34854 İstanbul, Turkey
[b] Complex Fluid Processing section, Process & Energy Department, Faculty of Mechanical, Engineering, Delft University of Technology, 2628, CB, Delft, the Netherlands

ARTICLE INFO

Editor: Guangming Jiang

Keywords:
Electrochemical separation
Boron removal
Cell design
Optimization
Kinetics and
Thermodynamics

ABSTRACT

Boron contamination of various water sources has been increasing in recent years and is receiving worldwide attention for its negative effects on the environment, wildlife, and humans; therefore, its removal is of utmost importance. Considering dwindling water sources and the possibility of the world population soon experiencing water scarcity, effective and innovative technologies must be developed to remove boron ions from water sources. The aim of the present study was to assess a sustainable separation process for the removal of boron ions using an electrochemical flow cell with symmetric redox-active polyvinyl ferrocene (PVF) functionalized carbon nanotube (CNT) electrodes using real-time measurements of the boron adsorption performance in continuous-flow mode while varying the flow rate, cell voltage, and boron concentration. A Box–Behnken experimental design (BBD) was used to improve boron adsorption. The adsorption isotherms, kinetics, and thermodynamics were investigated to further describe the adsorption process. The high R^2 value, calculated using a linear and nonlinear procedure, demonstrated that the Langmuir isotherm and pseudo-first order models fit quite well. The maximum adsorption of 60.61 mg/g was observed. The thermodynamic results illustrated that the adsorption of boron ions onto the PVF/CNT electrodes was spontaneous and endothermic under continuous flow mode.

1. Introduction

Boron is an element found in minerals such as borax and kernite. Its omnipresence in everyday products ranging from ceramics to semiconductors underscores strategic importance [1–3]. Boron is used as a micronutrient as well as, is commercially utilized within a wide range of areas, such as in the chemical, glass, ceramics, electronics, fertilizer, metallurgy, and textile industries [4,5]. Unfortunately, the widespread use of boron in aforementioned industries has led to elevated concentrations in both surface and groundwater resources [6,7]. Boron is generally found in nature as both boric acid and borate ion [8]. Owing to the high solubility of boric acid and borate salts easily dissolve in water, boron ions from waste streams can be found in water sources at high concentrations and they can accumulate in water resources posing environmental and health risks, especially when present in drinking water [9,10]. For example, the World Health Organization has identified 2.4 mg/L as the maximum acceptable boron concentration for drinking water; whereas, the European Union proposed an even lower of 1.0 mg/L [11–13]. At higher boron concentrations, adverse effects on the cardiovascular, coronary, nervous, and reproductive systems in humans have been reported [14,15]. In addition, boron concentrations are at different levels depending on the area of use [16,17]. For example, in the semiconductor industry, especially for chip production, high volumes of pure water are used, and the amount of boron contained in this water should be at a specific ppb level to prevent contamination on the surfaces of the chips [11]. In another area of use, high concentrations of boron are detrimental. For example, excess boron can not only reduce fruit yield but also result in premature ripening and massive leaf damage, which is why the boron concentrations in plant irrigation water should not exceed 1 ppm [18]. Thus, although the presence of boron in aqueous solution at low concentrations has positive effects on humans and the environment, high concentrations can cause serious problems. In addition, because of the increasing water demand and the continuing pollution of usable water resources, the decreasing worldwide water resources has become an important problem that must be addressed. When considered within this context, boron pollution in water becomes a very important environmental problem.

In response to the escalating concentrations of boron in surface waters and the need to address potential adverse consequences, effective and sustainable methods by which to remove boron from water must be

* Corresponding author at: Chemical Engineering Department, Faculty of Engineering, Marmara University, 34854 İstanbul, Turkey.
E-mail address: sevgi.polat@marmara.edu.tr (S. Polat).

https://doi.org/10.1016/j.jwpe.2024.106481
Received 8 October 2024; Received in revised form 28 October 2024; Accepted 3 November 2024
Available online 5 November 2024

developed. Several studies in the literature provide information on boron removal using different treatment methods, such as coagulation and sedimentation [19], adsorption [20–22], crystallization [23], ion exchange [24], membrane processes [25–27], electrodialysis [28] and electrocoagulation [29,30]. Among these separation processes, studies have shown that successful results for boron removal have especially been achieved by adsorption, electrocoagulation, and electrodialysis. Although still frequently used, these techniques also pose disadvantages because of the difficulty and cost in the regeneration processes of the adsorbents, the need for ion exchange resins, expensive membranes, and constant maintenance requirements. The drawbacks at the commercial levels include high energy requirements, low ion removal at low boron concentrations, and high operating costs; however, research has shown that some advanced separation technologies have been developed, tested, and applied that mitigate these drawbacks, one of which is electrochemistry. Pseudocapacitive deionization (PCDI) an electrochemical separation technique, uses redox-active compounds that are deposited on the surface of a carbon electrode to selectively capture ions. These organometallic compounds offer a feasible solution to the drawbacks facing the industry because the processes are fast, the electrical potential is controlled, and the process leaves a lower footprint and has positive modularity, scalability, and reversibility. In addition, with PCDI, no additional chemicals or solvents are needed for the regeneration process, which makes PCDI extremely useful for water economy and sustaining downstream waste [31–36].

In the present study, the polyvinyl ferrocene/carbon nanotube (PVF/CNT) electrodes were created and characterized electrochemically, structurally and morphologically. A large-scale electrosorption cell was designed for a system to operate in continuous flow mode to remove the boron ions from the aqueous solution. The system's performance was significantly improved using an experimental design as the adsorption characteristics of the boron ions on the PVF/CNT electrodes were investigated in detail. The present study provides information on electrochemically mediated separations that address resource recovery from the removal of boron ions from an aqueous solution.

2. Materials and methods

2.1. Materials

Polyvinyl ferrocene (PVF) was supplied from Polysciences. Multi-walled carbon nanotubes (CNTs) and anhydrous chloroform were analytically pure and purchased from Sigma Aldrich (Gillingham, UK). Potassium sulfate (K_2SO_4) and boric acid (H_3BO_3) were obtained from Merck (Darmstadt, Germany) and used without further post-treatment. Toray carbon paper (CP, TGP-H-60) was purchased from Alfa Aesar. Ultrapure water was used to prepare the solutions.

2.2. Experimental methods

The experiment comprised the following five stages: fabricating and characterizing of the PVF/CNT electrodes, designing an electrochemical flow cell, constructing a continuous-flow electrosorption system, optimizing the conditions for obtaining the highest efficiency of boron removal, and investigating the adsorption characteristics (i.e., isotherms, kinetics, and thermodynamics of the boron ions under continuous-flow conditions).

2.2.1. Fabrication and characterization of PVF/CNT electrodes

Toray carbon paper was used as the surface for the working electrode. The electrodes were fabricated by preparing a mixture of PVF and CNT electrodes in a mass ratio of 1:1 with 20 mL anhydrous chloroform used as the solvent. The mixture was thoroughly sonicated using the Bandelin ultrasound homogenizer HD 2200 for 1 h at 40 % amplitude to obtain a uniform homogenous slurry. The sonicated PVF/CNT solution was then ready for use, and the solution was drop-cast onto one side of the electrode surface, after which the electrodes were left to dry in an oven at 30 °C for 2 h. Two sizes of electrodes were constructed. First, 50 μL of the solution was drop-cast on a 1- by 1-cm electrode surface for electrochemical characterization. Second, 250 μL of the solution was drop-cast on a 5- by 5-cm electrode surface for flow-cell experiments.

For the electrochemical tests, three electrodes—a PVF/CNT, a platinum, and an Ag/AgCl as a reference—were used. Cyclic voltammetry (CV) measurements were conducted in a 0.1 M K_2SO_4 solution using a Biologic SP-200 potentiostat (5.0 mV/s) under an argon atmosphere at room temperature. The surface sites were activated when the total charge passed through ferrocene; therefore, the charge could be calculated by integrating the area under the anodic peak as determined using the Biologic EC-lab peak-analysis tool. Eq. (1) shows the relation between the charge and the measured current:

$$Q = \int_{t_1}^{t_2} I dt = \frac{1}{\nu}\int_{E_1}^{E_2} I dE \tag{1}$$

where Q is the charge (C), ν is the sweep rate (V/s) and E_1 and E_2 are the potentials where the anodic peak starts and ends (V).

In addition to the electrochemical analyses, the structural and morphological properties of the prepared PVF/CNT electrodes were identified via an X-ray diffraction instrument (XRD, Bruker D2 Phaser Tabletop Diffractometer), a JY Horiba LabRAM HR Raman spectrometer, and a scanning electron microscopy (FESEM, Thermo Scientific Apreo 2S).

2.2.2. Cell design and construction of continuous electrosorption system

The present study used the Rhinoceros 3D modelling software. As depicted in Figs. 1a and b, the cell comprised two resin plates placed parallel to each other, sandwiching two electrodes together as with a wall of the cell. The inside of the cell had one middle plate with an inner flow channel, a pair of carbon paper electrodes, and titanium current collectors. The electrodes were spaced by the middle plate, allowing for flow between them. In the present study, unlike classical flow cells, seven flow channels were designed within the middle plate to ensure that the feed solution passed through the electrode surface homogeneously while feeding the cell, thereby increasing boron removal efficiency. In addition, the flow channels increased the mass transfer through the channel by mixing the flowing feed solution while supporting the electrodes and ensuring there was no accidental connection between them, which would have led to a short circuit during operation. Because of the design of the flow channels, spacers were not necessary. Two titanium strips were applied to each electrode to function as current collectors. The cell was secured with bolts and the nuts were dispersed around the plates. The modular design of the electrochemical cell allowed for a wide variety of experiments, which enabled more studies on the effect of cell voltage and volume flow.

The boron adsorption and desorption values were measured using a constructed electrosorption system (Fig. 1c). The experimental setup comprised a programmable source meter, fully equipped (e.g., with electrodes and current collectors) electrochemical flow cell, peristaltic pump, conductivity sensor, pH probe, and data logging software. First, a channel was flushed with pure water, after which the boron solution was sent through the cell. The solution was continuously pumped from the influent container into the electrochemical flow cell using a peristaltic pump at a constant flow rate of 1.0 mL/min. After the solution emerged from the cell, both the conductivity and pH were measured using a sensor and pH electrode that were placed at the outlet port. The power supply ensured the mode of operation for the experiments using constant voltages (0.7, 1.0, and 1.3 V). A source meter was used to measure both the potential and electric current used. A 1.0-V charge was applied to the cell for 5 min followed by a discharge of −1.0 V for 5 min and repeated several times. Any changes to the current values were recorded. The samples were taken from the outlet flow at 5-s intervals, and boron concentration was determined using inductively coupled plasma atomic

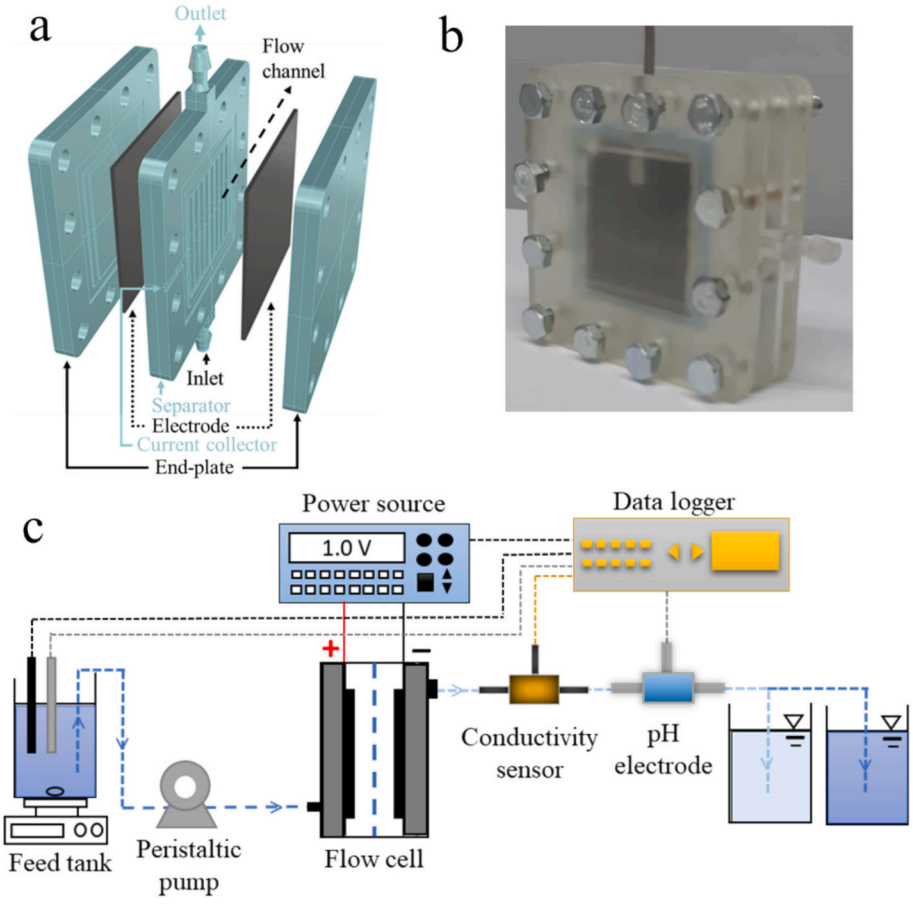

Fig. 1. (a) Exploded view three-dimensional (3D) drawing, and (b) photograph of the electrochemical cell. The cell comprised two resin plates, two electrodes, a separator, and current collectors. (c) Schematic of the boron electrochemical separation system with influent and effluent containers, the peristaltic pump, the electrochemical cell, a power source, and inline sensors including an electroconductivity sensor and a pH probe.

emission spectroscopy. Each experiment was cycled at least five times and repeated at least three times. The total cycle charge efficiency of the process, defined as the amount of boron removed per charge passed, was calculated as:

$$\Lambda = \frac{q_{boron}}{q_{charge}} = \frac{Q\int (C_{in} - C)dt}{\int Idt/F} \tag{2}$$

where C_{in} and C are the initial and final boron concentrations, Q is the volumetric flow rate, F is the Faraday constant.

In addition, to investigating the adsorption of the boron ions on the PVF/CNT electrodes, the experiments were conducted at a boron concentration of 10–100 mg/L, a contact time of 0–300 s, and a temperature of 20–40 °C. The amounts of boron ions per unit mass of adsorbent at equilibrium (q_e), and at each time interval (q_t), were calculated using the following equations:

$$q_e = \frac{(C_i - C_e) \times V}{W} \tag{3}$$

$$q_t = \frac{(C_i\text{-}C_t) \times V}{W} \tag{4}$$

Where C_i is the initial concentration and C_e is the equilibrium concentration of boron ion (mg/L). C_t is the concentration of the boron ions at any time (mg/L), W is the mass of adsorbent (g) and V is the solution volume (L).

2.2.3. Design-of-experiments approach

To investigate the effect of the various operating conditions on the efficiency of the cycle charge, the design-of-experiments approach was used. The flow rate (A), cell voltage (B), and boron concentration (C) were chosen as the input variables. A Box–Behnken design (BBD) [37] combined with the response surface method (RSM) was used to generate the experimental plan. As shown in Table S1, each condition was varied over three levels representing the upper, medium, and lower boundary of each parameter. The data representing the upper and lower limits of each factor were selected based on preliminary experiments. Based on RSM, 15 experiments with varying conditions were designed. A three-factor, three-level BBD was used as the basis of the experiments. Using Design Expert (https://www.statease.com/software/design-expert/), a multidimensional cube was created that comprised midpoints and central points (Eq. 5).

$$N = 2k(k-1) + C_0 = 2 \times 3(3-1) + 3 = 15 \tag{5}$$

where N is the number of the experiments, k is the number of independent variables and C_0 is the replicate number of central point. The levels and ranges of the variables used in the present study are listed in Table S1. Following the experiments, we used a second-order polynomial regression model equation to determine the mathematical relationship between the response function and the process variable. The general form of this equation is as follows:

$$Y = \beta_0 + \sum_{i=1}^{k}\beta_i X_i + \sum_{i=1}^{k}\beta_{ii}X_i^2 + \sum_{i_{i=1}}^{k}\sum_{j>1}^{k}\beta_{ij}X_iX_j \tag{6}$$

where Y shows the predicted response, β_0 is the constant term, β_i is the linear coefficient, β_{ii} is the quadratic coefficient, and β_{ij} is the interaction

coefficient.

The software analyzed the experimental designs and generated the surface plots. Analysis of variance (ANOVA) was used to evaluate significance of the operation parameters and/or the combined effect by their interactions of those parameters. R^2 and the *F*-test were used to validate the model by comparing the calculated values with those predicted.

3. Results and discussion

3.1. PVF/CNT electrode characterization

Because the electrochemical characterization of a synthesized electrode determines how it functions, its cyclic voltammetry (CV) was used to conduct the electrochemical characterization of the PVF/CNT electrode that was created (Fig. 2a and b).

At first, the basic forms of the CV curves for the electrodes containing PVF and those containing PVF/CNT appeared similar; however, two key distinctions were noted. First, by adding CNT to the PVF film, the peak potentials for ferrocene oxidation were altered, which caused a shift in the peak potentials of both the anode and cathode. In addition, the peak current for both the oxidation and reduction was much higher with the PVF/CNT electrodes than with the electrodes containing only PVF or CNT. In the PVF/CNT electrode voltammogram, the anodic peak current was 2.3 mA at 0.52 V and the cathodic peak current was −2.1 mA at 0.18 V. In contrast, in the PVF electrode voltammogram, the anodic peak current was 0.29 mA at 0.41 V and cathodic peak was −0.16 mA at 0.29 V. The increase in the current response in the PVF/CNT electrode resulted from incorporation of highly conductive carbon nanotubes into the PVF film. These nanotubes reduced resistance of the polymer matrix to the charge transfer, which enabled the ferrocene oxidation and reduction to be more effective. Second, the higher peaks using the PVF/CNT electrode indicated that its performance was highly dependent on ferrocene deposition onto the electrode surface [38]. These deposits adsorbed boron ions from the solution. The number of active sites was directly related to the area under the anodic peak curve, which indicated that its charge was proportional to the amount of PVF deposited. The PVF/CNT co-deposited electrode had the highest charge at 81.3 ± 5.2 mC. Fig. 2b shows the electrochemical performance of the PVF/CNT electrode. The results show that the voltammograms of five cycles are very similar, indicating that the fabricated electrodes were reversible and stable in the electrolyte.

In addition to electrochemical characterization, XRD and Raman analyses were performed to structurally characterize PVF/CNT electrodes, and the results are shown in Fig. 2c and d. The main diffraction peak was observed at 2θ = ~26°, which was the result of the (002) graphite facet of the carbon paper [39,40]. All diffraction peaks corresponded to those of carbon paper and the intensity and sharpness of the peaks were similar to each other, indicating that the structure was not changed. Typical peaks of PVF were not found, which could be the result of the production of thin film layers on the electrode surface and the dominant effect of carbon paper peaks. XRD analysis results were supported with Raman results. In the Raman spectra shown in Fig. 2d, there were two prominent peaks at ~1350 cm^{-1} and 1580 cm^{-1} corresponding to D and G peaks respectively. The results were consistent with those reported from earlier studies [41–44]. In addition to electrochemical and structural tests, the morphological characterization of the produced electrodes was examined. The scanning electron microscope (SEM) images are shown in Fig. 2e. Similar to that in earlier research [45,46], the surface of the untreated carbon paper electrode was composed of smooth carbon fibers. Upon examination, the electrodeposited carbon paper/CNT electrode showed nearly the same morphology as the untreated carbon paper electrode; consequently, the coating of the carbon surface was essentially unaffected by the application of CNT alone. Nonetheless, the electrodeposited carbon paper/PVF electrode differed from the untreated carbon paper electrode. There was an uneven layer of polymer composed of hollow structures that covered the surface, which was anticipated as a polymer's nature changed to one of oxidation and solvophobicity on the electrode surface. After examining SEM of the electrodeposited PVF/CNT electrodes, it was observed that the electrode surface exhibited homogeneous dispersion, smoothness, and nearly uniform porosity together with micropores of consistent size that were connected by a three-dimensional framework and encircled by a conformal polymer covering. The CNTs and ferrocene moieties interacted to form and distribute a stable film onto the substrate, after which the electrons moved swiftly from the carbon fiber substrate to the polymer's redox-active core [41,47].

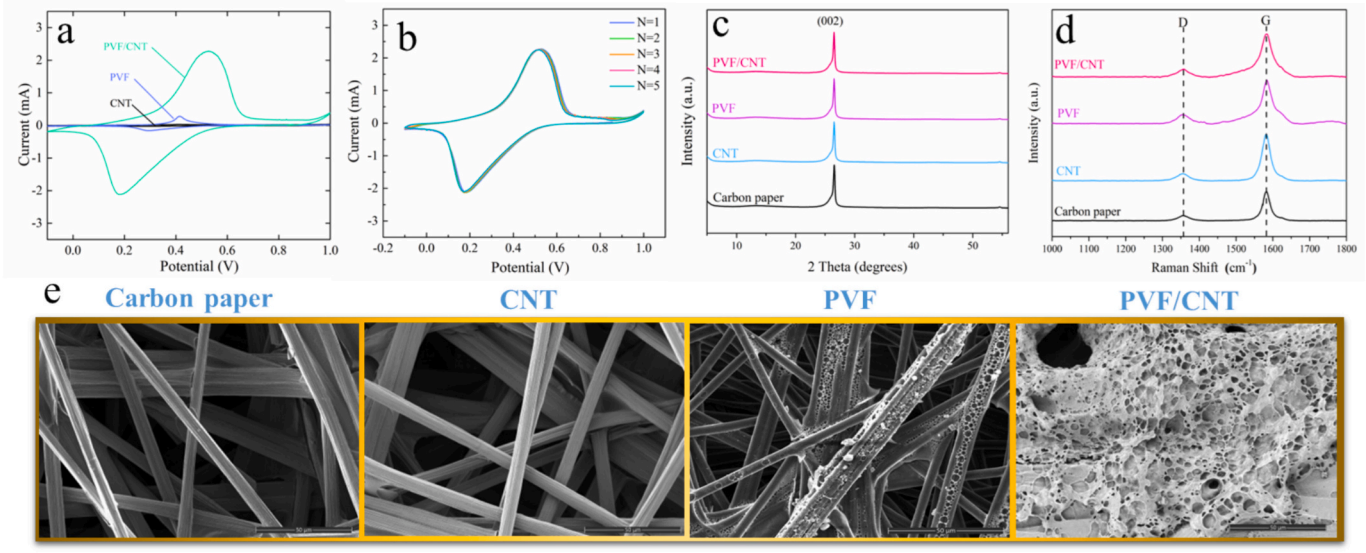

Fig. 2. (a) Cyclic voltammograms of individual CNT (black line), PVF (blue line), and PVF/CNT (green line) electrodes at the scan rate of 5 mV/s. (b) Electrochemical stability of the prepared PVF/CNT electrode. (c) XRD patterns and (d) Raman spectra of the fabricated electrodes. (e) Scanning electron microscopy (SEM) images of untreated carbon paper electrode, carbon paper electrode treated by electrochemical oxidation in the CNT/chloroform dispersion, PVF/chloroform dispersion, and PVF/CNT chloroform dispersion. (For interpretation of the references to colour in this figure legend, the reader is referred to the web version of this article.)

3.2. Flow system results

After fabrication and characterization of the PVF/CNT electrodes at the small scale (2 by 1 cm), the performance of our electrochemical cell (8 by 8 cm) was tested under realistic conditions at constant voltage and continuous flow of 10 ppm boron concentration. A schematic illustration of the flow cell with redox-active PVF/CNT electrodes is shown in Fig. 3.

The basic operation principle of this cell can be separated into three steps as follows: (1) uncharged, (2) adsorption/charging, and (3) desorption/discharging. First, the cell was fed with at a constant flow rate of 1.0 mL/min. During the uncharged step, redox-active moieties were present on both the anode and cathode, after which the electrodes were connected to the power source and charged at 1.0 V for 5 min for adsorption and discharged at −1.0 V for 5 min for desorption. This cycle was repeated throughout the experiment for five consecutive cycles to ensure a dynamic steady state. During the electrochemical measurement, the voltage between the electrodes was stepped to 1.0 V for 5 min, and the redox moieties on the anode were oxidized to ferrocenium with a net positive charge. The applied charge caused anions to be adsorbed from the influent through hydrogen bonding and electrostatic attraction to control the adsorption strength [48]. After this charging phase, the applied potential was removed and the electrodes regenerated by setting the voltage difference to −1.0 V, applying a reverse potential.

The applied voltage step and current response are illustrated in Fig. 4a, and the profiles of the effluent concentration and pH of boron ions are shown in Fig. 4b. The curves show typical adsorption/desorption behavior. From Fig. 4b, it is observed that applying the potential across the electrodes resulted in a drop in boron concentration as the electrodes became saturated over time. After saturation, the concentration of boron gradually increased back to its initial value. The boron concentration in the effluent stream stabilized and reached equilibrium in <300 s. The experiments were repeated no less than five times, reaching the same equilibrium time with each experiment; therefore, this time interval was considered in the experiments when applying the potential cycles. Moreover, Fig. 4b shows a sharp increase in boron concentration when applying a potential −1.0 V for 5 min. In this case, the adsorbed ions from the earlier step were desorbed back into the outlet flow, which was why the high concentration was observed. As the electrodes were fully regenerated, boron concentration returned to its initial value. The behavior of the five adsorption/desorption cycles was similar, which indicated that a dynamic steady state had been reached. The effluent's conductivity and pH were continuously recorded during the experiments to determine the cell's performance. The variation in pH was also recorded during the electrosorption process, with a change between 8.5 and 10.8. An increase in pH was observed during the adsorption stage; whereas, the pH decreased during the desorption stage. In addition to the experiments with an adsorption potential at 1 V, experiments were conducted at varying potentials ranging from 0.7 to 1.30 V at a constant flow rate of 1 mL/min. Fig. 4c, d and e compare the voltage/current profiles, and their corresponding concentration change, and the charge efficiencies with respect to the applied potential. Fig. 4c indicates that a higher applied voltage increased the current and provided a larger charge efficiency of the flow cell. At 1.6 V, the charge efficiency reached the highest value of 84.7 %. Fig. 4f illustrates the prolonged cycling performance of the PVF/CNT electrodes and the profile kept stable after 10 h of cycling, showing the high reversibility of the electrodes.

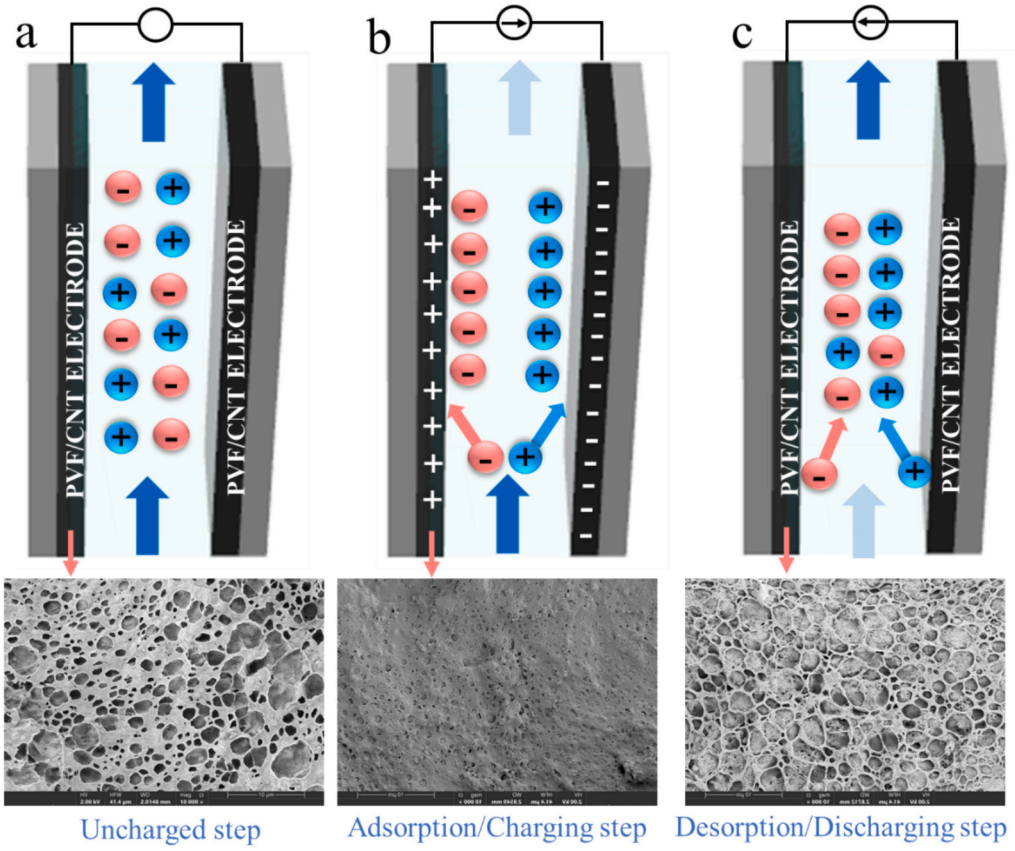

Fig. 3. Schematic representation of the flow cell with redox-active PVF/CNT electrodes for (a) uncharged step, (b) adsorption step, and (c) desorption step during the electrosorption process. Scanning electron microscopy (SEM) images of the PVF/CNT electrodes obtained treated by electrochemical oxidation for (a) uncharged step, (b) adsorption step, and (c) desorption step.

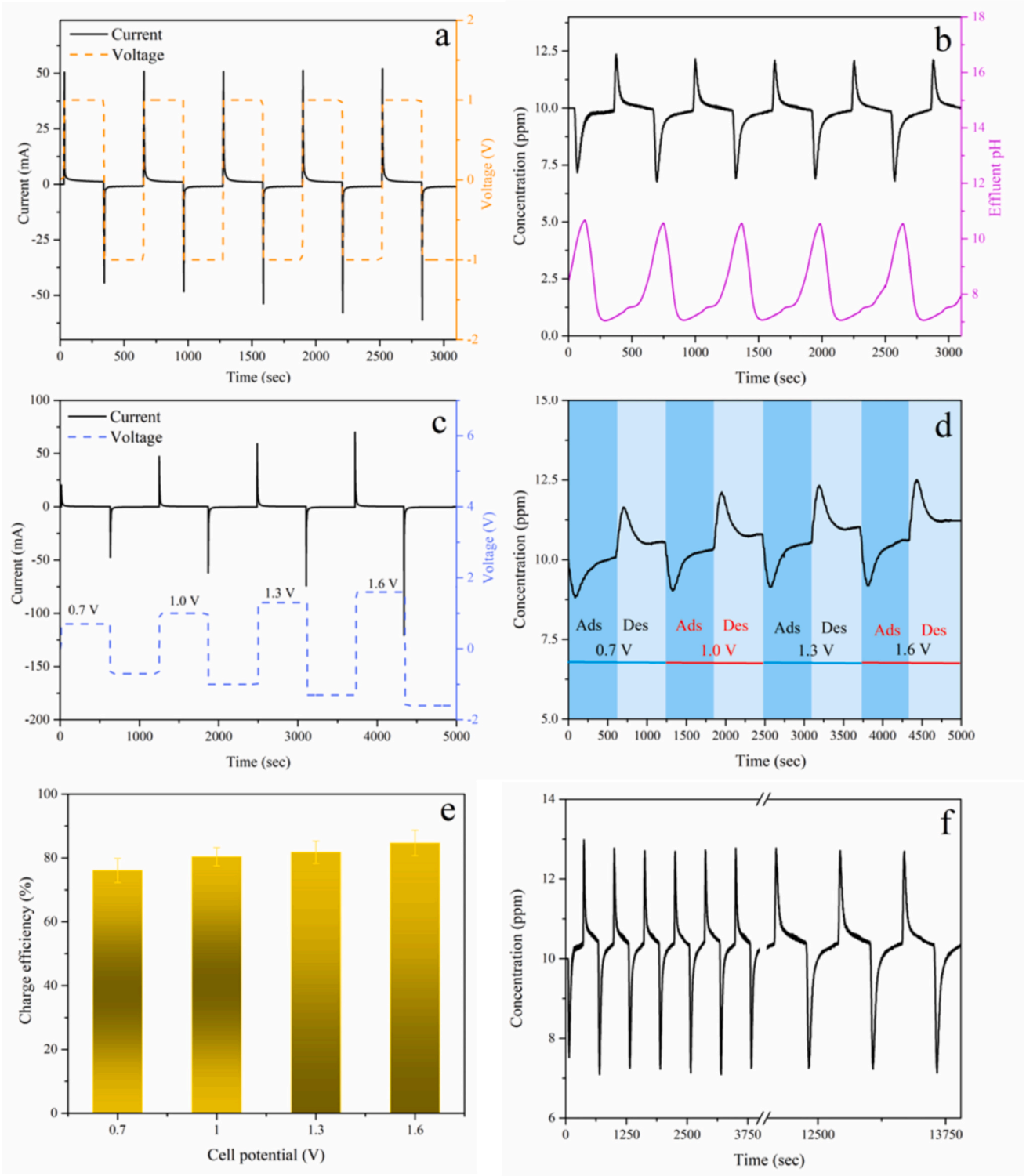

Fig. 4. (a) Current and voltage profiles and (b) the effluent concentration and pH of boron ions under constant charging at 1.0 V and discharging at −1.0 V cell voltage in 10 ppm boron solution. (c) Current and voltage profiles, (d) the effluent concentration, and (e) the charge efficiencies with respect to the applied potential under different charging and discharging cell voltage in 10 ppm boron solution. (f) Cycling performance of PVF/CNT electrode pair under constant charging and discharging cell voltage.

3.3. Experimental design results

A BBD experimental design was used to investigate the effects of three independent variables—flow rate (A), cell voltage (B), and boron concentration (C)—on the response function to determine the conditions that maximized the process efficiency and, thus, boron adsorption performance. The designed experiments and their corresponding measured responses are presented in Table S2. Based on these results, the relationship between the independent variables and the predicted response (i.e., total cycle charge efficiency [CE]) was formulated as follows:

$$Y_{CE} = 72.67 - 9.54A + 7.17B - 3.34C - 0.97AB + 1.50AC - 0.43BC - 2.01A^2 - 2.93B^2 - 3.61C^2 \quad (7)$$

The coded coefficients were calculated using Design Expert (https://www.statease.com/software/design-expert/), and their values and signs showed the significance level of the operation conditions. The positive sign in this equation indicated the synergistic effect of the factors on the output response. It can be concluded from the developed second-order polynomial equation that the flow rate imposed a more significant effect on the charge efficiency when compared to other operating conditions in which a lower flow rate increased the charge efficiency. The cell voltage was the second significant factor affecting the charge efficiency of the electrosorption process, while the boron concentration had the least significant impact.

ANOVA was used to evaluate the significance of the quadratic model and identify the terms that had the most impact on the response (Table 1). Accordingly, there is an inverse relationship between the F value and *p*-value, and the analysis showed that the model was statistically significant (i.e., $p < 0.05$). The obtained *p*-values indicated that the flow rate (A) and cell voltage (B) were significant factors that affected the total cycle charge efficiency with the least p-value (i.e., < 0.001) compared to concentration (C). The effect of combined interaction with the two factors, i.e., factor AB, factor AC, and factor BC showed insignificant effects with *p*-value >0.1. The quadratic terms affected the cycle efficiency in the following order: $C^2 > B^2 > A^2$.

When using the *F* test for significance, a high *F* value showed that the regression equation adequately accounted for much of the output variation. In the present study, the F-value, which shows that the model was statistically significant, was calculated as 64.59 and the p-value was 0.0001, indicating that there was only a 0.01 % chance that noise influenced the F-value. Moreover, the model determination coefficient, R^2, of 0.9761 for the total cycle charge efficiency further showed a good correlation between the measured and predicted responses. Because the predicted values were similar to the experimental values (Fig. 5a), BBD was suitable for both. Fig. 5b provides the perturbation plot that was used to examine the simultaneous effect on total cycle charge efficiency based on the three factors. As a variable moved from a reference point, the efficiency was determined; no other factors were involved. The sharp curvature observed for each variable indicated a significant effect on the maximum cycle charge efficiency.

Using RSM, the effects of the independent variables on the total cycle efficiency were plotted in three-dimensional (3D) response surface plots and two-D (2D) contour plots and the results are given in Fig. 6. The main aim of the response surface is to monitor variables efficiently for the optimum values to maximize the response. The best response range can be calculated by analyzing the plots. Based on these 3D and 2D plots together, it can be concluded that increasing the flow rate and boron concentration resulted in a decreased charge efficiency. As the applied cell voltage increased, a comparable increase in the total cycle charge efficiency was observed. It was also observed that as the flow rate of the feed solution decreased from 10 to 1 mL/min, the cycle efficiency increased from 64.3 to 87.0 % at constant boron concentration.

Table 1
Analysis of variance results of the response surface quadratic model for total cycle charge efficiency (%).

Source	Sum of Squares	*df*	Mean Square	*F*-Value	*p*-value Prob > F
Model	1325.33	9	147.26	64.59	0.0001
A-Flow rate	*727.71*	1	*727.71*	*319.19*	< 0.0001
B- Cell voltage	*411.84*	1	*411.84*	*180.65*	< 0.0001
C-Electrolyte concentration	*89.11*	1	*89.11*	*39.09*	*0.0015*
AB	*3.80*	1	*3.80*	*1.67*	*0.2530*
AC	*9.00*	1	*9.00*	*3.95*	*0.1037*
BC	*0.72*	1	*0.72*	*0.32*	*0.5978*
A^2	*14.89*	1	*14.89*	*6.53*	*0.0509*
B^2	*31.77*	1	*31.77*	*13.94*	*0.0135*
C^2	*48.07*	1	*48.07*	*21.09*	*0.0059*
Residual	11.40	5	2.28	–	–
Lack of fit	10.39	3	3.46	6.88	0.1295
R^2	0.9915				

Notes: Adj $R^2 = 0.9761$, pred $R^2 = 0.8739$, adequate precision = 27.112, standard deviation = 1.51; significance parameter, affecting total cycle charge efficiency response.

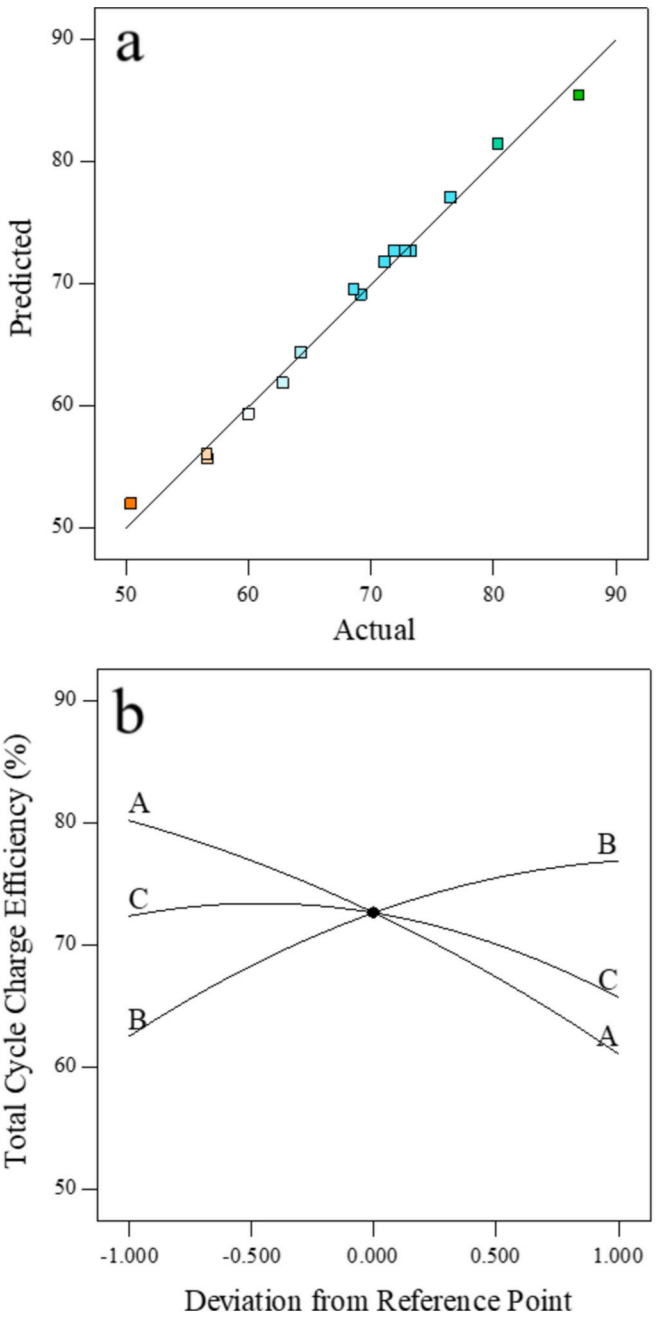

Fig. 5. (a) The plot of predicted versus actual values and (b) the perturbation plot of each factor (A: Flow rate, B: Cell voltage, and C: Boron concentration) for total cycle charge efficiency (%).

3.4. Adsorption characteristics

3.4.1. Effect of boron concentration, contact time, and temperature on the adsorption process

Under optimized conditions (i.e., highest efficiency), the adsorption

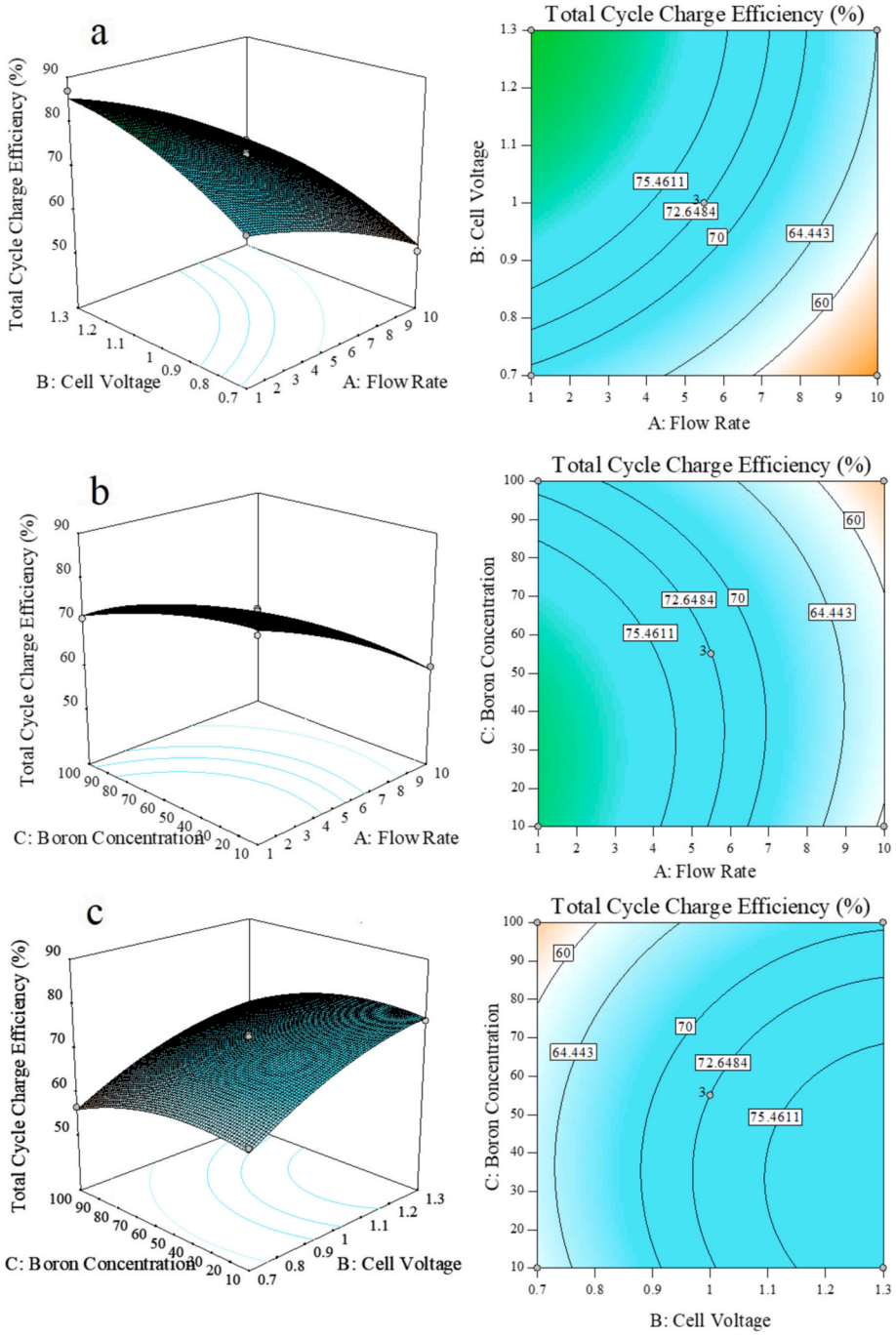

Fig. 6. Three-dimensional (3D) response surface plots and two-D (2D) contour plots showing the effects of (a) flow rate and cell voltage, (b) flow rate and boron concentration, and (c) cell voltage and boron concentration on the total cycle charge efficiency (%).

characteristics of boron on the electrode surface were investigated in detail. In addition, the characterization of the electrodes used under continuous flow conditions was investigated using SEM and Brunauer–Emmett–Teller (BET) analysis. When the SEM images were examined in Fig. 3, it was observed that the surface of the PVF/CNT electrodes comprised homogeneously distributed porous structures. The BET surface area was found to be 546.2 m^2/g which indicates the porous characteristics of the fabricated PVF/CNT electrodes. As a result of the adsorption process, boron ions completely filled these holes. When the surfaces of the electrodes obtained as a result of the desorption process were examined, it was observed that homogeneously distributed porous structures were reformed. The energy-dispersive X-ray spectroscopy analysis results also proved that boron ions were adsorbed onto the electrode surfaces. (Fig. S1).

In this section, where the adsorption characteristics of boron ions onto PVF/CNT electrodes was studied using the electrochemical separation method, the effect of boron concentration and contact time on the adsorption process was also determined as a function of temperatures ranging from 20 °C to 40 °C. The results are shown in Fig. S2. As shown in S2, temperature changes affected the equilibrium capacity of the adsorbent for boron ions. Regardless of boron concentrations, the adsorption efficiency increased when the temperature increased. These results can be explained by the increase in the molecular diffusion rate and in the active sites on the surface at higher temperatures. This situation also revealed that the adsorption process was endothermic. The maximum adsorption capacities were determined as 25.97, 36.88 and

47.65 mg/g for 100 ppm boron concentrations at 20, 30, and 40 °C temperature, respectively. The time was also another important parameter affecting boron adsorption onto the PVF/CNT electrodes. It was determined that at the initial stage, the adsorption process was fast, and a large amount of boron ions adsorbed onto the electrode surfaces in the first 90 s. Then, it reached equilibrium within 120 s and after this time, no distinctive increase or decrease was observed in the amount of adsorbed boron ions per unit mass of adsorbent. The initial rapid adsorption rate may have occurred to due to availability of a large number of vacant sites and the absence of internal diffusion resistance. After this time, the very low increase in additive uptake that was observed can be attributed to the low number of surface-active sites on adsorbent.

3.4.2. Adsorption isotherms

Adsorption isotherms are used to describe interactions between adsorbate and adsorbent when in equilibrium and provide fundamental information on the adsorption process. Various isotherm models have been proposed in the published literature. In the present study, the most frequently used isotherm models were Langmuir, Freundlich, and Temkin. The Langmuir isotherms assume monolayer adsorption with homogeneous interactions with a solute. The Freundlich isotherm is associated with multilayer adsorption onto the heterogeneous adsorbate surface [49–51]. The Temkin model was also used to investigate the adsorption isotherm in the present study. This isotherm predicts that adsorption energy decreases linearly with surface coverage because of the interaction between adsorbent particles and the adsorbate [52]. Table S3 summarizes linear expressions for these models and their parameters. The isotherm parameters obtained from the Langmuir, Freundlich and Temkin models at different temperatures were calculated with the help of the linear expressions, and their respective results are given in Table 2. The maximum adsorption capacity obtained from the Langmuir isotherm was 35.21, 57.14, and 60.61 mg/g at 20, 30, and 40 °C, respectively. In other words, in agreement with the results shown in Fig. S2, the amount of boron ions adsorbed increased with the increase in the temperature. The R_L values in the Langmuir model at different temperatures were between 0.2065 and 0.1259, which indicated that the adsorption of the boron ions onto the PVF/CNT electrodes was favorable. The Freundlich model also supported these results. According to the Freundlich isotherm models, the value of n indicates adsorption favorability. If $n > 1$, the adsorption isotherm is favorable. In the present study, n was 1.680, 1.429, and 1.720 at 20, 30, and 40 °C, respectively, which indicated favorable adsorption of the boron ions onto the PVF/CNT electrodes. In addition, a nonlinear regression analysis was conducted for all models of adsorption isotherms, and the isotherm fitting was plotted using nonlinear equations (Fig. 7). Data obtained through the linear and non-linear methods were similar, and they supported each other. The Langmuir model should be selected as the most appropriate isotherm model for describing the adsorption equilibrium behavior of boron ions on PVF/CNT electrodes. According to this result, there was a homogenous distribution of boron ion adsorption onto the electrode surface on the active sites plus a monolayer sorption of adsorbate onto the outer surface.

Table 2
Isotherm constants for boron adsorption at different temperatures.

Isotherms	20 °C	30 °C	40 °C
Langmuir			
q_m (mg/g)	35.21	57.14	60.61
K_L (L/mg)	0.0384	0.0320	0.0694
R_L	0.2065	0.2378	0.1259
R^2	0.9997	0.9919	0.9999
Freundlich			
K_F ((mg/g)(L/mg)$^{1/n}$)	2.187	2.368	5.287
n	1.680	1.429	1.720
R^2	0.9443	0.9556	0.9601
Temkin			
K_T (L/mg)	0.4332	0.4257	0.8759
B	7.5037	11.498	12.367
R^2	0.9799	0.9817	0.9733

3.4.3. Adsorption kinetics

An adsorption kinetic study provides important details on the adsorption rate, performance of the adsorbent used, and mass transfer mechanisms. Determining the adsorption kinetics of a material is essential when designing an effective adsorption system and selecting optimum operating conditions. To precisely determine the adsorption kinetics of boron ions onto PVF/CNT electrodes, several kinetic frameworks, such as the pseudo-first-order (PFO), pseudo-second-order (PSO), and intraparticle diffusion kinetic models, were developed to provide comprehensive information on the mass transfer of boron ions. The pseudo-first-order model or Lagergren's kinetic model assumes a reversible interaction with an established equilibrium between adsorbate and the surface of the adsorbent. PSO model is designated for evaluating the chemisorption kinetics. It is also assumed that adsorption is influenced by the chemical potentials of both the adsorbent surface and the adsorbates [53,54]. Apart from these models, the intraparticle diffusion, or Morris–Weber kinetic, model takes into account the diffusion effects of the adsorption kinetics. The model provides information on the adsorption processes that comprise instantaneous adsorption onto the external service; gradual adsorption diffused inside the pores; and equilibration of the process, during which the adsorbates slowly move from inside the larger pores into micropores [55]. Table S4 shows the linearized equations and the parameters of these adsorption models.

The parameters for the PFO, PSO, and intraparticle diffusion models at different temperatures and their respective correlation coefficients are provided in Table S5. Given that R^2 indicates a relationship between calculated and experimental values, this coefficient was used to determine the best-fit model. The results indicated that the PFO model was more compatible with the experimental data (Table S5), which suggests that pore diffusion on the PVF/CNT electrodes, not chemisorption domination, was the decisive step in the boron adsorption process. Table S5 also provides the intraparticle diffusion rate constants, k_p, at different temperatures. The data showed that k_p values were directly related to temperatures and that temperature influenced the mobility of the adsorbate (i.e., increased temperatures increased mobility) based on the endothermic properties of the adsorbate. Adsorption kinetics was also studied using nonlinear kinetic models. The kinetic data that were observed to be the best fit were calculated using the PFO model (Fig. 7). Data gathered using the linear method were compatible with those using the nonlinear method.

3.4.4. Adsorption thermodynamics

In addition to the analysis of adsorption kinetics, proper assessment of thermodynamic parameters, such as standard Gibbs free-energy change (ΔG°), the enthalpy change (ΔH°), and the entropy change (ΔS°), could provide in-depth information about the nature of adsorption (i.e., the nature of adsorbent–adsorbate interactions) and adsorption types and mechanisms (i.e., either chemical or physical). The thermodynamic parameters can be calculated according to the thermodynamic laws using the following equations:

$$\Delta G^{\circ} = -RTlnK_L \tag{8}$$

$$\Delta G^{\circ} = \Delta H^{\circ} - T\Delta S^{\circ} \tag{9}$$

$$lnK_L = \frac{\Delta S^{\circ}}{R} - \frac{\Delta H^{\circ}}{RT} \tag{10}$$

where R is a universal gas constant (8.3144 J/mol.K), and T is absolute

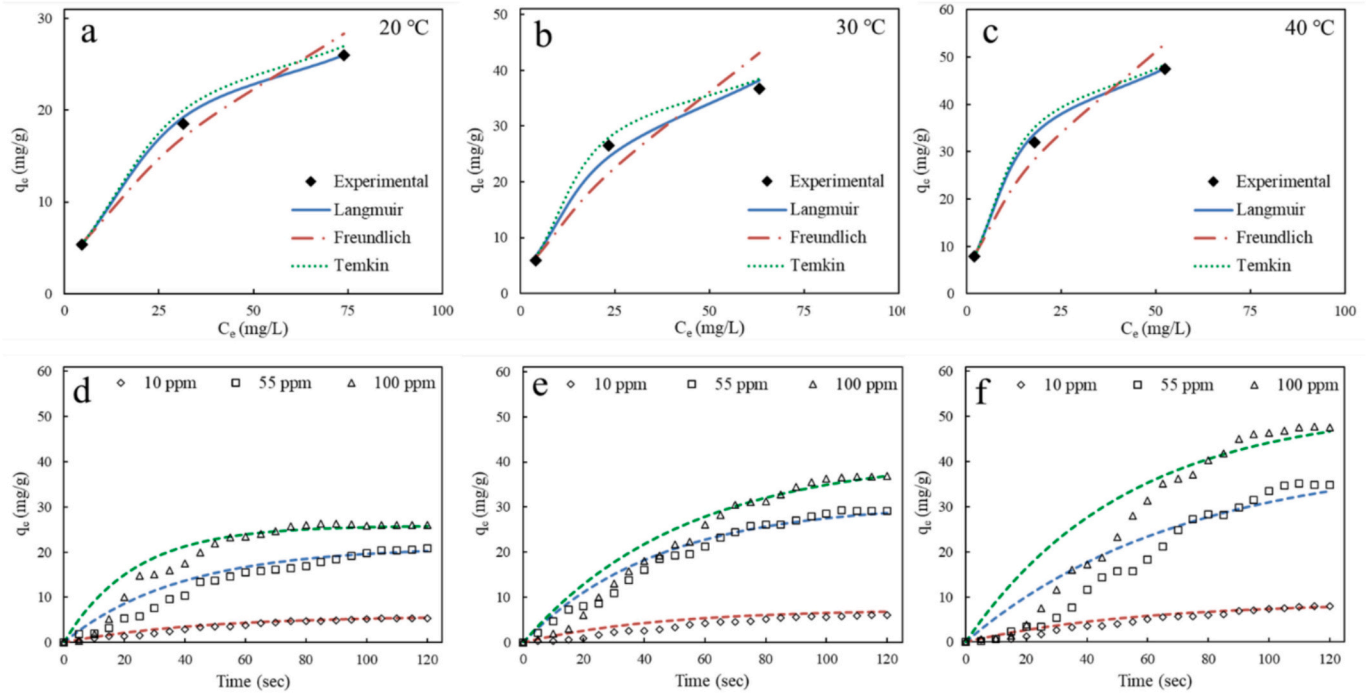

Fig. 7. Fit of adsorption isotherm models by non-linear procedure for boron removal (a) 20 °C, (a) 30 °C, and (c) 40 °C. Fit of pseudo-first-order adsorption kinetics model by non-linear procedure for boron removal (d) 20 °C, (e) 30 °C, and (f) 40 °C.

temperature in Kelvin (K). Each energy function has its physical sense as follows: ΔH° indicates the heat effect of adsorption process and ΔG° is the minimum isothermal work necessary to load the adsorbent to a given level. An understanding of the behavior of adsorption entropies helps to determine how the adsorbed molecules are packed together. Table 3 shows the calculated thermodynamic parameters (ΔG°, ΔH°, and ΔS°) for boron adsorption. The values of the Gibbs free energy change, a critical factor in determining the degree of adsorption spontaneity, were between −14.29 and − 21.03 kJ/mol at 20–40 °C. As observed from Table 3, the ΔH° was positive within the range of 36.12–44.52 kJ/mol, which indicates not only an endothermic process but an increase in the adsorption capacity of the adsorbent with increased temperatures (see also Fig. S2). Concurrently, ΔS° provided information on system disorders during the adsorption process. The magnitude and sign of ΔS° during the adsorption process indicated whether the organization of the adsorbate at the solid interface became more random. The positive value of ΔS° at 172.0–209.4 kJ/mol indicated an increased disorderliness at the solid/solution interface during the adsorption of boron ions.

Table 3
Thermodynamic parameters for boron adsorption at different temperatures.

Parameters					
Boron concentration	T °C	ΔG° kJ/mol	ΔS° J/mol K	ΔH° kJ/mol	R^2
10 ppm	20	−16.84	209.4	44.52	
	30	−18.93			0.9964
	40	−21.03			
55 ppm	20	−15.60	196.4	41.95	
	30	-17.56			0.9797
	40	−19.53			
100 ppm	20	−14.29	172.0	36.12	0.9828
	30	−16.01			
	40	−17.73			

4. Conclusions

This work successfully demonstrates how boron ions can be removed from aqueous solution using PVF/CNT redox electrodes. The fabricated electrodes were characterized based on their morphology, structural properties, and electrochemical and electrosorption performance. SEM image showed that PVF/CNT electrodes had a porous structure with a high BET surface area. The performance of the constructed flow platform was improved by optimizing the conditions using an experimental design. The BBD results indicated that the higher boron adsorption efficiency can be achieved at a lower flow rate under continuous flow conditions. The optimal operation conditions were 1.0 mL/min, 1.3 V, and 55 ppm boron concentration. Moreover, the adsorption characteristics of the boron ions on PVF/CNT electrodes were determined in terms of isotherms, kinetics and thermodynamics. The Langmuir isotherm model and pseudo-first-order kinetic model were the most suitable models to describe the boron adsorption process under continuous flow mode. The thermodynamic data revealed the endothermic and spontaneous nature of the adsorption process. The present study may pave the way for designing and operating an electrochemical system for boron removal on a larger scale.

CRediT authorship contribution statement

Sevgi Polat: Writing – review & editing, Writing – original draft, Visualization, Methodology, Investigation, Conceptualization. **Hüseyin Burak Eral:** Supervision.

Declaration of competing interest

The authors declare that they have no known competing financial interests or personal relationships that could have appeared to influence the work reported in this paper.

Acknowledgements

This study was supported by Scientific and Technological Research Council of Turkey (TUBITAK) under the Project No: 123M952. S.Polat thanks to TUBITAK for their supports.

Appendix A. Supplementary data

Supplementary data to this article can be found online at https://doi.org/10.1016/j.jwpe.2024.106481.

Data availability

Data will be made available on request.

References

[1] Z.B. Öcal, M.S. Öncel, B. Keskinler, A. Khataee, A. Karagündüz, Sustainable treatment of boron industry wastewater with precipitation-adsorption hybrid process and recovery of boron species, Process. Saf. Environ. Prot. 182 (2024) 719–726, https://doi.org/10.1016/j.psep.2023.12.006.

[2] B.N.S. Al-dhawi, S.R.M. Kutty, A.H. Jagaba, N. Aminu, A.H. Birniwa, G.A.M. Al-Shawesh, N.M.Y. Almahbashi, Boron adsorption from aqueous solutions through column study: desorption mechanisms, regeneration techniques, and kinetic insights, Desalin. Water Treat. 320 (2024) 100586, https://doi.org/10.1016/j.dwt.2024.100586.

[3] B.N.S. Al-dhawi, S.R.M. Kutty, A.M. Alawag, N.M.Y. Almahbashi, F.A.H. Al-Towayti, A. Algamili, N. Aminu, A.B.A. Al-Mekhlafi, A.H. Birniwa, A.H. Jagaba, Optimal parameters for boron recovery in a batch adsorption study: synthesis, characterization, regeneration, kinetics, and isotherm studies, Case Stud. Chem. Environ. Eng. 8 (2023) 100508, https://doi.org/10.1016/j.cscee.2023.100508.

[4] J. Niu, D. Zhang, J. Shen, H. Chu, C. Wang, Y. Wei, Poly (ethylene imine)-mediated dihydroxy-functionalized resin with enhanced adsorption capacity for the extraction of boron from salt lake brine, J. Environ. Chem. Eng. 12 (2024) 113779, https://doi.org/10.1016/j.jece.2024.113779.

[5] N. Yu, H. Jiang, Z. Luo, W. Geng, J. Zhu, Boron adsorption using NMDG-modified polypropylene melt-blown fibers induced by ultraviolet grafting, Polymers (Basel). 15 (2023) 1–21, https://doi.org/10.3390/polym15102252.

[6] D. Rosa, D. Cifaldi, L. Di Palma, Boron removal from wastewater via coordinative adsorption assisted by Fenton-induced Oxoprecipitation/flocculation, Chem. Eng. J. 498 (2024) 155572, https://doi.org/10.1016/j.cej.2024.155572.

[7] K.C. Kim, N. Il Kim, T. Jiang, J.C. Kim, C.I. Kang, Boron recovery from salt lake brine, seawater, and wastewater – a review, Hydrometallurgy 218 (2023) 106062, https://doi.org/10.1016/j.hydromet.2023.106062.

[8] M.A. Nellessen, P. Gasda, L. Crossey, E. Peterson, A. Ali, J. Zhang, W. Zhou, M. Hao, M. Spilde, H. Newsom, N. Lanza, A. Reyes-Newell, S. Legett, D. Das, D. Delapp, C. Yeager, A. Labouriau, S. Clegg, R.C. Wiens, Boron adsorption in clay minerals: implications for martian groundwater chemistry and boron on Mars, Icarus 401 (2023) 115599, https://doi.org/10.1016/j.icarus.2023.115599.

[9] S. Vasudevan, J. Lakshmi, Electrochemical removal of boron from water: adsorption and thermodynamic studies, Can. J. Chem. Eng. 90 (2012) 1017–1026, https://doi.org/10.1002/cjce.20585.

[10] J. Ulatowska, K. Szewczuk-Karpisz, I. Polowczyk, Evaluation of the effect of Polyethylenimine on boron adsorption by soil minerals, ChemPhysChem 25 (2024) 1–9, https://doi.org/10.1002/cphc.202400055.

[11] C. Bai, H. Zhang, Q. Luo, X. Ye, H. Liu, Q. Li, J. Li, Z. Wu, Boron separation by adsorption and flotation with mg–Al-LDHs and SDBS from aqueous solution, Chinese J. Chem. Eng. 61 (2023) 192–200. doi:https://doi.org/10.1016/j.cjche.2023.02.009.

[12] A.Y.A.H. Ahmed, H. Al Najar, N.A. Ghalwa, Removal of boron from aqueous solution through adsorption process using cationic surfactant (CTAB)-modified kaolin clay, Desalin, Desalin. Water Treat. 295 (2023) 133–141, https://doi.org/10.5004/dwt.2023.29586.

[13] A. Yagmur Goren, Y.K. Recepoglu, A. Karagunduz, A. Khataee, Y. Yoon, A review of boron removal from aqueous solution using carbon-based materials: An assessment of health risks, Chemosphere 293 (2022) 133587, https://doi.org/10.1016/j.chemosphere.2022.133587.

[14] M. Bryjak, J. Wolska, N. Kabay, Removal of boron from seawater by adsorption-membrane hybrid process: implementation and challenges, Desalination 223 (2008) 57–62, https://doi.org/10.1016/j.desal.2007.01.202.

[15] E. Avraham, M. Noked, A. Soffer, D. Aurbach, The feasibility of boron removal from water by capacitive deionization, Electrochim. Acta 56 (2011) 6312–6317, https://doi.org/10.1016/j.electacta.2011.05.037.

[16] J. Yao, S. Zhang, Z.C. Yan, D.S. Li, Y. Wang, W. An, H.Y. Yang, Effect of protonation and deprotonation on oxygen-containing groups functionalized graphene for boron adsorption removal, Desalination 583 (2024) 117692, https://doi.org/10.1016/j.desal.2024.117692.

[17] L. Yang, Y. Li, L. Guo, P. Ma, Z.Y. Leong, J. Wang, H.Y. Yang, Economical-effective purification of brackish water through an integrated capacitive desalination & boron adsorption system, Desalination 572 (2024) 117152, https://doi.org/10.1016/j.desal.2023.117152.

[18] Y. Tanaka, Chapter 4 electro-deionization, Membr. Sci. Technol. 12 (2007) 437–460, https://doi.org/10.1016/S0927-5193(07)12018-0.

[19] Y. Liu, T. Takaya, A. Ohuchi, Boron removal from wastewater via coagulation sedimentation with ettringite: An experimental and mechanism study, Desalin. Water Treat. 58 (2017) 435–441, https://doi.org/10.5004/dwt.2017.11434.

[20] N.N. Xia, H.Y. Zhang, Z.H. Hu, F. Kong, F. He, A functionalized bio-based material with abundant mesopores and catechol groups for efficient removal of boron, Chemosphere 263 (2021) 128202, https://doi.org/10.1016/j.chemosphere.2020.128202.

[21] J.Y. Lin, N.N.N. Mahasti, Y.H. Huang, Recent advances in adsorption and coagulation for boron removal from wastewater: a comprehensive review, J. Hazard. Mater. 407 (2021) 124401, https://doi.org/10.1016/j.jhazmat.2020.124401.

[22] X. Qiu, K. Sasaki, T. Hirajima, K. Ideta, J. Miyawaki, One-step synthesis of layered double hydroxide-intercalated gluconate for removal of borate, Sep. Purif. Technol. 123 (2014) 114–123, https://doi.org/10.1016/j.seppur.2013.12.031.

[23] J.Y. Lin, N.N.N. Mahasti, Y.H. Huang, Fluidized-bed crystallization of barium perborate for continuous boron removal from concentrated solution: supersaturation as a master variable, Sep. Purif. Technol. 278 (2022) 119588, https://doi.org/10.1016/j.seppur.2021.119588.

[24] N. Biçak, N. Bulutçu, B.F. Şenkal, M. Gazi, Modification of crosslinked glycidyl methacrylate-based polymers for boron-specific column extraction, React. Funct. Polym. 47 (2001) 175–184, https://doi.org/10.1016/S1381-5148(01)00025-6.

[25] S. Ghiasi, T. Mohammadi, M.A. Tofighy, Hybrid nanofiltration thin film hollow fiber membranes with adsorptive supports containing bentonite and LDH nanoclays for boron removal, J. Membr. Sci. 655 (2022) 120576, https://doi.org/10.1016/j.memsci.2022.120576.

[26] S. Wang, S. Bing, H. Zhang, Y. Zhou, L. Zhang, C. Gao, Surface engineering design of polyamide membranes for enhanced boron removal in seawater desalination, J. Membr. Sci. 651 (2022) 120425, https://doi.org/10.1016/j.memsci.2022.120425.

[27] Y.P. Tang, L. Luo, Z. Thong, T.S. Chung, Recent advances in membrane materials and technologies for boron removal, J. Membr. Sci. 541 (2017) 434–446, https://doi.org/10.1016/j.memsci.2017.07.015.

[28] F. Guesmi, I. Louati, C. Hannachi, B. Hamrouni, Optimization of boron removal from water by electrodialysis using response surface methodology, Water Sci. Technol. 81 (2020) 293–300, https://doi.org/10.2166/wst.2020.105.

[29] E.H. Ezechi, M.H. Isa, S.R.M. Kutty, A. Yaqub, Boron removal from produced water using electrocoagulation, Process. Saf. Environ. Prot. 92 (2014) 509–514, https://doi.org/10.1016/j.psep.2014.08.003.

[30] M.H. Isa, E.H. Ezechi, Z. Ahmed, S.F. Magram, S.R.M. Kutty, Boron removal by electrocoagulation and recovery, Water Res. 51 (2014) 113–123, https://doi.org/10.1016/j.watres.2013.12.024.

[31] S. Liao, C. Xue, Y. Wang, J. Zheng, X. Hao, G. Guan, A. Abuliti, H. Zhang, G. Ma, Simultaneous separation of iodide and cesium ions from dilute wastewater based on PPy/PTCF and NiHCF/PTCF electrodes using electrochemically switched ion exchange method, Sep. Purif. Technol. 139 (2015) 63–69, https://doi.org/10.1016/j.seppur.2014.11.003.

[32] H. Yoon, J. Lee, S. Kim, J. Yoon, Review of concepts and applications of electrochemical ion separation (EIONS) process, Sep. Purif. Technol. 215 (2019) 190–207, https://doi.org/10.1016/j.seppur.2018.12.071.

[33] A. Suresh, G.T. Hill, E. Hoenig, C. Liu, Electrochemically mediated deionization: a review, Mol. Syst. Des. Eng. 6 (2021) 25–51, https://doi.org/10.1039/d0me00090f.

[34] N. Kim, J. Jeon, R. Chen, X. Su, Electrochemical separation of organic acids and proteins for food and biomanufacturing, Chem. Eng. Res. Des. 178 (2022) 267–288, https://doi.org/10.1016/j.cherd.2021.12.009.

[35] X. Su, A. Kushima, C. Halliday, J. Zhou, J. Li, T.A. Hatton, Electrochemically-mediated selective capture of heavy metal chromium and arsenic oxyanions from water, Nat. Commun. 9 (2018), https://doi.org/10.1038/s41467-018-07159-0.

[36] N. Kim, J. Jeon, J. Elbert, C. Kim, X. Su, Redox-mediated electrochemical desalination for waste valorization in dairy production, Chem. Eng. J. 428 (2022) 131082, https://doi.org/10.1016/j.cej.2021.131082.

[37] G.E.P. Box, D.W. Behnken, Some new three level designs for the study of quantitative variables, Technometrics 2 (1960) 455–475, https://doi.org/10.1080/00401706.1960.10489912.

[38] S. Polat, R. Kortlever, H.B. Eral, Ultrasound-promoted preparation of polyvinyl ferrocene-based electrodes for selective formate separation: experimental design and optimization, Ultrason. Sonochem. 89 (2022) 106146, https://doi.org/10.1016/j.ultsonch.2022.106146.

[39] T. Zhang, X. Zhu, D.D. Ye, R. Chen, Y. Zhou, Q. Liao, Cyclic voltammetry electrodeposition of well-dispersed Pd nanoparticles on carbon paper as a flow-through anode for microfluidic direct formate fuel cells, Nanoscale 12 (2020) 20270–20278, https://doi.org/10.1039/d0nr05134a.

[40] Y. Fu, A. Manthiram, Silicon nanoparticles supported on graphitic carbon paper as a hybrid anode for Li-ion batteries, Nano Energy 2 (2013) 1107–1112, https://doi.org/10.1016/j.nanoen.2013.09.004.

[41] X. Mao, G.C. Rutledge, T.A. Hatton, Polyvinylferrocene for noncovalent dispersion and redox-controlled precipitation of carbon nanotubes in nonaqueous media, Langmuir 29 (2013) 9626–9634, https://doi.org/10.1021/la401440w.

[42] N. Lachman, X. Sui, T. Bendikov, H. Cohen, H.D. Wagner, Electronic and mechanical degradation of oxidized CNTs, Carbon N. Y. 50 (2012) 1734–1739, https://doi.org/10.1016/j.carbon.2011.12.009.

[43] B. Anis, H. El Fllah, T. Ismail, W.M. Fathallah, A.S.G. Khalil, O.M. Hemeda, Y. A. Badr, Preparation, characterization, and thermal conductivity of polyvinyl-formaldehyde/MWCNTs foam: a low cost heat sink substrate, J. Mater. Res. Technol. 9 (2020) 2934–2945, https://doi.org/10.1016/j.jmrt.2020.01.044.

[44] A.K. Singh, N. Yasri, K. Karan, E.P.L. Roberts, Electrocatalytic activity of functionalized carbon paper electrodes and their correlation to the Fermi level derived from Raman spectra, ACS Appl. Energy Mater. 2 (2019) 2324–2336, https://doi.org/10.1021/acsaem.9b00180.

[45] S. Guo, M.J. Kim, J.C. Siu, N. Von Windheim, K. Gall, S. Lin, B.J. Wiley, Eight-fold intensification of electrochemical Azidooxygenation with a flow-through electrode,

ACS Sustain. Chem. Eng. 10 (2022) 7648–7657, https://doi.org/10.1021/acssuschemeng.2c01525.
[46] Y. Qi, X. Chen, D. Huo, H. Liu, M. Yang, C. Hou, Simultaneous detection of Cd2+ and Pb2+ in food based on sensing electrode prepared by conductive carbon paper, rGO and CoZn·MOF (CP-rGO-CoZn·MOF), Anal. Chim. Acta 1220 (2022) 339812, https://doi.org/10.1016/j.aca.2022.339812.
[47] X. Su, H.J. Kulik, T.F. Jamison, T.A. Hatton, Anion-selective redox electrodes: electrochemically mediated separation with heterogeneous organometallic interfaces, Adv. Funct. Mater. 26 (2016) 3394–3404, https://doi.org/10.1002/adfm.201600079.
[48] F. He, A. Hemmatifar, M.Z. Bazant, T.A. Hatton, Selective adsorption of organic anions in a flow cell with asymmetric redox active electrodes, Water Res. 182 (2020) 115963, https://doi.org/10.1016/j.watres.2020.115963.
[49] M.A. Al-Ghouti, D.A. Da'ana, Guidelines for the use and interpretation of adsorption isotherm models: a review, J. Hazard. Mater. 393 (2020) 122383, https://doi.org/10.1016/j.jhazmat.2020.122383.
[50] X. Yuan, S. Ma, C. Zhao, X. Chen, Y. Zhou, S. Xi, S. Liu, Cadmium (II) ion adsorption of an industrial liquid waste-derived ferric oxide loaded with chitosan: parameters optimization, isotherms, kinetics and thermodynamics, Desalin. Water Treat. 319 (2024) 100578, https://doi.org/10.1016/j.dwt.2024.100578.
[51] T. Nizam, K.A. Krishnan, A. Joseph, R.R. Krishnan, Isotherm, kinetic and thermodynamic modelling of liquid phase adsorption of the heavy metal ions Zn (II), Pb(II) and Cr(VI) onto MgFe2O4 nanoparticles, Groundw. Sustain. Dev. 25 (2024) 101120, https://doi.org/10.1016/j.gsd.2024.101120.
[52] R.F. Abbas, M.J.M. Hassan, A.M. Rheima, Adsorption of fast green dye onto Fe3O4 MNPs and GO/Fe3O4 MNPs synthesized by photo-irradiation method: isotherms, thermodynamics, kinetics, and reuse studies, Sustain. Chem. Environ. 6 (2024) 100104, https://doi.org/10.1016/j.scenv.2024.100104.
[53] Q. Hu, R. Lan, L. He, H. Liu, X. Pei, A critical review of adsorption isotherm models for aqueous contaminants: curve characteristics, site energy distribution and common controversies, J. Environ. Manag. 329 (2023) 117104, https://doi.org/10.1016/j.jenvman.2022.117104.
[54] H.V.T. Luong, T.P. Le, T.L.T. Le, H.G. Dang, T.B.Q. Tran, A graphene oxide based composite granule for methylene blue separation from aqueous solution: adsorption, kinetics and thermodynamic studies, Heliyon 10 (2024) e28648, https://doi.org/10.1016/j.heliyon.2024.e28648.
[55] Q. Hu, S. Ma, Z. He, H. Liu, X. Pei, A revisit on intraparticle diffusion models with analytical solutions: underlying assumption, application scope and solving method, J. Water Process Eng. 60 (2024) 105241, https://doi.org/10.1016/j.jwpe.2024.105241.